IEEE Open Journal of
Antennas and Propagation

Received 4 May 2021; accepted 11 August 2021. Date of publication 24 August 2021; date of current version 14 September 2021.

Digital Object Identifier 10.1109/OJAP.2021.3107444

A Systematic Comparison of Near-Field Beamforming and Fourier-Based Backward-Wave Holographic Imaging

SEBASTIAN PAUL [1,2], FABIAN SCHWARTAU [1], MARKUS KRUECKEMEIER [1], REINHARD CASPARY [2], CARSTEN MONKA-EWE [1], JOERG SCHOEBEL [1,2] (Senior Member, IEEE), AND WOLFGANG KOWALSKY [1,2]

[1]Microwave Engineering Lab, Institut für Hochfrequenztechnik, Technische Universität Braunschweig, 38106 Braunschweig, Germany

[2]Cluster of Excellence PhoenixD (Photonics, Optics, and Engineering—Innovation Across Disciplines), Leibniz Universitat Hannover, 30167 Hannover, Germany

CORRESPONDING AUTHOR: S. PAUL (e-mail: sebastian.paul@ihf.tu-bs.de)

This work was supported in part by the Deutsche Forschungsgemeinschaft (DFG, German Research Foundation) under Germany's Excellence Strategy within the Cluster of Excellence PhoenixD (EXC 2122, Project ID 390833453); in part by the German Research Foundation; and in part by the Open Access Publication Funds of Technische Universität Braunschweig.

ABSTRACT In this paper we show the equivalence of near-field beamforming and backward-wave reconstruction algorithm. The proof is carried out analytically with two different approaches, using the principle of stationary phase from a signal processing point of view and the angular spectrum representation as an electromagnetic point of view. A comparison of the time complexity of the near-field beamforming and backward-wave reconstruction algorithm is given. A detailed discussion of the constraints required for a digital implementation is presented, leading to limitations for the chosen system parameters, especially for the backward-wave reconstruction approach. An exemplarily scenario is simulated and processed, confirming the found equivalence between the two very different approaches of image reconstruction. An additional measurement with a 120 GHz radar showcases the capabilities of both algorithms and validates our findings.

INDEX TERMS Near-field beamforming, backward-wave reconstruction, radar imaging.

I. INTRODUCTION

IN THIS paper we compare two commonly used algorithms for two-dimensional image reconstruction from coherently collected raw data. The first algorithm is a near-field narrow-band phase shift delay-and-sum beamformer [1, p. 31]. As we will see later in this paper, near-field beamforming can either be interpreted as a cross-correlation between the measured aperture data and the sensor's point spread function or, equivalently, as a convolution with a matched filter derived from the sensor's point spread function. The second algorithm is a backward-wave reconstruction algorithm [2]–[4], which exploits computationally efficient FFTs. This algorithm is widely used in holographic imaging [4], [5].

The first important contribution made by this paper is to show that these two very different algorithms, which will be discussed further in Section II, are in fact identical from a mathematical point of view.

We present two different approaches for showing the equivalence of these spatial and spatial frequency domain algorithms. One approach discussed in Section III-A is to show that the transfer function of the matched filter used in backward-wave propagation can be obtained by Fourier-transforming the sensor's time-reversed, complex conjugate point spread function by means of the principle of stationary phase, which is widely used in synthetic aperture radar processing [6], [7]. The second approach discussed in this paper, which will be presented in Section III-B, is to decompose the integral describing near-field beamforming into forward and inverse Fourier transforms. In order to do so, an angular spectrum representation is used to expand a spherical wave into a continuous spectrum of planar Eigenmodes.

The second important contribution made by this paper are several conditions connecting, for example, the sample interval and the given/chosen apertures. This derivation will be presented in Section IV. It will be shown that in a discrete implementation of the backward-wave reconstruction algorithm the constructed transfer function needs to be designed slightly larger in both the spatial and spatial frequency domain compared to the theoretically required size due to the leakage effect. We introduce two scaling factors to mathematically represent this scaling and solve the negative influence of the leakage effect [8, p. 219].

The fact that near-field beamforming and backward-wave reconstruction are equivalent algorithms has several important consequences. Firstly, the Fourier-based backward-wave reconstruction algorithm can be viewed as a computationally efficient implementation of near-field beamforming. Secondly, images reconstructed by near-field beamforming in fact can be considered as "correct" reference images for the backward-wave reconstruction algorithm.

Lastly, predictable sidelobe behavior corresponding to si-functions can be achieved in an implementation of backward-wave reconstruction if the presented approach is used, which guarantees the equivalence of the two algorithms. If in contrast the aperture size and aperture sampling interval are chosen incorrectly, distorted sidelobe patterns are observed.

In order to demonstrate the equivalence of the two algorithms and to show the practical relevance of our findings, we will process both simulated and measured data using implementations of the two algorithms. In Section V, simulated data for a point target will be processed while in Section VI measurement data for a small corner reflector mimicking a point target is processed. For both datasets, the results obtained using the two algorithms show outstanding agreement.

II. DESCRIPTION OF THE ALGORITHMS

Consider the imaging geometry depicted in Fig. 1. In order to obtain an image of the target distribution, i.e., the reflectivity function $g(x', y')$ within the target plane at $z = |z_0|$, a two-dimensional aperture located within the aperture plane at $z = 0$ is scanned. The raw radar data obtained during the process of aperture scanning can be denoted as a convolution

$$f(x, y) = g(x', y') * p(x, y). \tag{1}$$

of the reflectivity function $g(x', y')$ and the sensor's point spread function

$$p(x, y) = e^{-j2k\sqrt{x^2+y^2+|z_0|^2}}, \tag{2}$$

where $*$ is the convolution operator and $k = 2\pi/\lambda$. The exponent denotes the round trip phase observed between the sensor position $\langle x, y, z = 0\rangle$ within the aperture plane and the point target position $\langle x', y', z = |z_0|\rangle$ within the target / image plane.

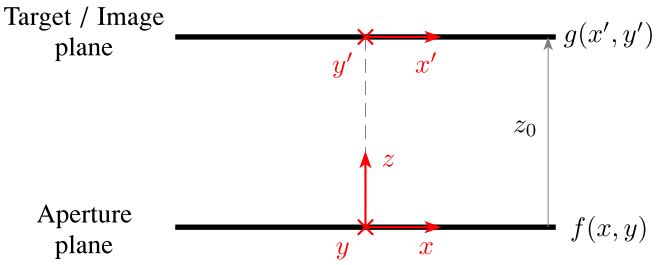

FIGURE 1. Conceptual representation of the imaging geometry.

The two algorithms compared in this paper provide means to reconstruct the image, i.e., the reflectivity function $g(x', y')$, from the raw radar data $f(x, y)$ and will be briefly summarized in the following.

A. NEAR-FIELD BEAMFORMING

The first algorithm to be discussed is near-field beamforming, which is an algorithm operating in the spatial domain. For the discussion in this paper an algorithm for a continuous defined aperture is needed. In the usual literature, however, the argumentation is mostly application-oriented with discrete antenna positions of a radar system in mind, as it is the case in [9].[1] Our approach is based on the one-dimensional far-field beamforming described for continuous apertures in [11]. Equivalently to (1) in [11], a two-dimensional and near-field capable formulation of continuous aperture beamforming can be formulated as[2]:

$$g(x', y') = \int\int_{-\infty}^{\infty} f(x, y)\, e^{j2k\sqrt{(x-x')^2+(y-y')^2+|z_0|^2}}\, \mathrm{d}x\, \mathrm{d}y. \tag{3}$$

The integral (3) can be interpreted as a cross-correlation

$$g(x', y') = p(x, y) \star f(x, y) \tag{4}$$

of the raw radar data with the sensor's point spread function $p(x, y)$ of (2) with $\star$ being the cross-correlation operator[3] or as a convolution

$$g(x', y') = h(x, y) * f(x, y) \tag{5}$$

of the raw radar data with a matched filter whose impulse response denotes

$$h(x, y) = p^*(-x, -y) = e^{+j2k\sqrt{x^2+y^2+|z_0|^2}}. \tag{6}$$

While the continuous domain notation used in the equations so far is useful for showing the equivalence of the two algorithms in Section III, the underlying concept of near-field beamforming is explained best for a discrete implementation such as is shown in Fig. 2.

1. Reference [9] describes the general case of a delay-and-sum beamformer, which is applicable for near- and far-field conditions. Other sources, like [1, p. 31] or [10, p. 9ff], describe only the special case of far-field conditions for the delay-and-sum beamformer.

2. This is achieved by substituting the far-field approximation $x \cos\theta$ with the near-field equivalent $\sqrt{(x - x')^2 + (y - y')^2 + |z_0|^2}$.

3. Note the difference between convolution $(*)$ and correlation $(\star)$.

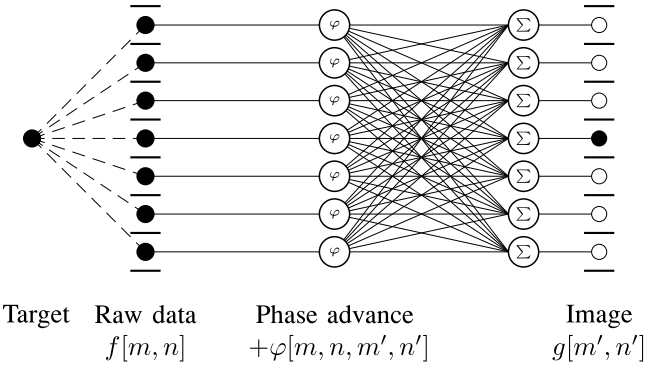

FIGURE 2. Reconstruction by near-field beamforming.

For every sensor position within the aperture, which corresponds to a complex-valued pixel $f[m,n]$ in the raw data, a well-known round trip phase delay between the sensor and a point target at a location corresponding to the pixel $g[m',n']$ to be reconstructed is observed.[4] As is illustrated by Fig. 2, the individual pixels are reconstructed by compensating this phase delay by means of a suitable phase advance and subsequent summation of all phase-corrected pixel values.

As a consequence, the near-field beamforming algorithm requires four nested loops for the reconstruction of a two-dimensional image, which makes the algorithm computationally expensive for aperture data with a large number of points.

B. BACKWARD-WAVE RECONSTRUCTION

The second algorithm to be discussed in this paper is backward-wave reconstruction, which is a holographic algorithm performing image reconstruction in the spatial frequency domain. In short, the algorithm can be denoted [4] as

$$g(x',y') = \mathcal{F}^{-1}\left\{e^{+jk_z|z_0|}\mathcal{F}\{f(x,y)\}\right\}, \tag{7}$$

where $\mathcal{F}$ and $\mathcal{F}^{-1}$ denote forward and inverse two-dimensional Fourier transforms as is illustrated in Fig. 3.

Equation (7) can be interpreted as a matched filtering operation by means of fast convolution with a filter having a transfer function

$$H(k_x,k_y) = e^{+jk_z|z_0|} \tag{8}$$

where

$$k_z^2 = 4k^2 - k_x^2 - k_y^2. \tag{9}$$

From (9) it is obvious that the value for k_z will become imaginary, if $k_x^2+k_y^2 > 4k^2$. This is a well known problem [2] and can be solved by either choosing adequate system parameters or working with a complex k_z. A complex k_z will cause $H(k_x,k_y)$ to be damped exponentially for values of $k_x^2+k_y^2 > 4k^2$. Complex values of k_z represent evanescent waves, which are not propagating and cannot be measured by a physical setup [2].

4. The described system is a mono-static radar, meaning that transmitter and receiver are always at the same position.

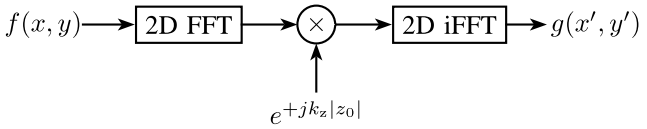

FIGURE 3. Backward-wave reconstruction algorithm, which employs two-dimensional FFTs.

III. EQUIVALENCE OF BEAMFORMING AND BACKWARD-WAVE RECONSTRUCTION

In the following, we will now show the equivalence of the two algorithms introduced in the previous section. Two different approaches can be followed in order to demonstrate the equivalence of the two algorithms.

The first approach takes a signal processing point of view and strives to show that (7) is in fact the fast convolution equivalent of the spatial domain convolution (3). In order to do so, the principle of stationary phase is used to show that (8) is the Fourier transform of (6).

The second approach is closely related to electromagnetic theory and employs an angular spectrum representation in order to decompose the spatial domain reconstruction integral (3) into forward and inverse Fourier transforms, giving a form equivalent to (7). This approach is somewhat related to the derivation of the backward-wave reconstruction algorithm presented in [4].

A. PROOF OF EQUIVALENCE USING THE PRINCIPLE OF STATIONARY PHASE

In order to show the equivalence of the two algorithms from a signal processing point of view, we wish to calculate the Fourier transform

$$H(k_x,k_y) = \iint e^{+j2k\sqrt{x^2+y^2+|z_0|^2}} e^{-jk_x x}\mathrm{d}x\, e^{-jk_y y}\mathrm{d}y \tag{10}$$

of the matched filter's point spread function (6). For the two algorithms to be equal, this Fourier transform must yield (8).

The inner integral, that is, the Fourier transform w.r.t. x can be solved using the principle of stationary phase, which is briefly reviewed in Appendix A. By comparing (10) with (38), the phase function $\phi_x(x)$ can be identified. In order to determine the stationary point, the first derivative

$$\phi_x'(x) = 2k\frac{x}{\sqrt{x^2+y^2+|z_0|^2}} - k_x \tag{11}$$

of the phase function is required, from which the stationary point

$$x_0 = k_x\frac{\sqrt{y^2+|z_0|^2}}{\sqrt{4k^2-k_x^2}} \tag{12}$$

satisfying $\phi_x'(x) = 0$ is calculated. Using (38), (10) can be rewritten as

$$H(k_x,k_y) = \int e^{j\sqrt{y^2+|z_0|^2}\sqrt{4k^2-k_x^2}}\, e^{-jk_y y}\mathrm{d}y, \tag{13}$$

when ignoring the constant scaling factor.

The second integration, which is the Fourier transform w.r.t. y, is again carried out using the principle of stationary phase. By comparing (38) with (13), the phase function $\phi_y(y)$ is identified. Its derivative denotes

$$\phi_y' = \frac{y}{\sqrt{y^2 + |z_0|^2}}\sqrt{4k^2 - k_x^2} - k_y, \tag{14}$$

which provides the stationary point

$$y_0 = k_y \frac{|z_0|}{\sqrt{4k^2 - k_x^2 - k_y^2}}. \tag{15}$$

satisfying $\phi_y'(y_0) = 0$. Using (38), the final form of the PSF's Fourier transform

$$H(k_x, k_y) = e^{+j\sqrt{4k^2 - k_x^2 - k_y^2}|z_0|} = e^{+jk_z|z_0|}, \tag{16}$$

where $k_z^2 = 4k^2 - k_x^2 - k_y^2$, is found.

Having shown that (8) is in fact the Fourier transform of (6), it immediately becomes obvious that (7) is the spatial frequency domain implementation, namely a fast convolution, of the spatial domain convolution (3).

B. PROOF USING AN ANGULAR SPECTRUM REPRESENTATION

In order to demonstrate the equivalence of the algorithms from an electromagnetics point of view, we consider the correlation integral (3)

$$g(x', y') = \iint_{-\infty}^{\infty} f(x, y)\; e^{j2k\sqrt{(x-x')^2 + (y-y')^2 + |z_0|^2}}\, \mathrm{d}x\, \mathrm{d}y$$

again.

The exponential term contained within this integral in fact represents the field distribution of an inward-traveling (i.e., divergent) spherical wave emitted by a point source located at $\langle x', y', z' = |z_0|\rangle$ within the target plane $z' = |z_0|$.

In order to decompose the above integral into forward and inverse Fourier transforms, this spherical wave is now expanded for planar wave functions by means of an angular spectrum representation (56), which is discussed in great detail in Appendix B.

In this context, two important points have to be observed: Because the exponential function in (3) describes a round-trip phase rather than the phase advance between a point source and an observation point, it contains an additional factor of 2, which is not present in (56). In order to use (56) for the expansion of (3), this factor of 2 has to be added to the exponent of the left side of (56) and the separation condition (44) has to be modified accordingly for the right side and becomes $4k^2 = k_x^2 + k_y^2 + k_z^2$, which immediately yields (9).

In addition, it has to be noted that in (56) the $1/r$ term describing spherical spread loss as well as the $2\pi/k_z$ term, which also represents a distance-dependent amplitude factor, have been omitted. This is permissible because image reconstruction is performed primarily based on the phase information, while the amplitude is almost constant.

Using the angular spectrum representation (56) of the spherical wave, (3) can be rewritten as

$$g(x', y') = \frac{j}{(2\pi)^2} \iint_{-\infty}^{\infty} f(x, y) \iint_{-\infty}^{\infty} e^{j(k_x(x'-x) + k_y(y'-y) + k_z|z_0|)}\, \mathrm{d}k_x\, \mathrm{d}k_y\, \mathrm{d}x\, \mathrm{d}y, \tag{17}$$

where we let $z = 0$ and $z' = |z_0|$ in (56).

By exploiting the linearity of the integrals and rearranging the exponential terms, this expression can rewritten as

$$g(x', y') = \frac{j}{(2\pi)^2} \iint_{-\infty}^{\infty} e^{+jk_z|z_0|} \iint_{-\infty}^{\infty} f(x, y) e^{-jk_x x} e^{-jk_y y}\, \mathrm{d}x\, \mathrm{d}y\; e^{jk_x x'} e^{jk_y y'}\, \mathrm{d}k_x\, \mathrm{d}k_y, \tag{18}$$

where we can identify the inner integral as a (forward) Fourier transform and the outer integral as an inverse Fourier transform. In short, this can be written[5] as

$$g(x', y') = \mathcal{F}^{-1}\left\{e^{+jk_z|z_0|}\mathcal{F}\{f(x, y)\}\right\} \tag{19}$$

which is exactly the reconstruction formula (7) of the backward-wave algorithm.

C. TIME COMPLEXITY ANALYSIS

It is assumed that the aperture and image plane are of equal size and have the same number of samples (N_x and N_y). The computational complexity of the FFT used in the backward wave reconstruction algorithm from (19) is $\mathcal{O}(N_x N_y \log(N_x N_y))$ [12, p. 913]. Considering the near-fiAeld beamforming algorithm from (3), a straightforward implementation requires a total of four nested for-loops. Regardless of what computational operations are performed in the most inner loop, these operations are independent of N_x and N_y and thus their complexity is constant. Therefore, the implementation of the near-field beamforming results in a computational complexity of $\mathcal{O}(N_x^2 N_y^2)$. As a result, the backward wave reconstruction algorithm can be implemented in a computationally more efficient way than the near-fiAeld beamforming algorithm thanks to the use of the FFT.

IV. IMPLEMENTATIONAL ASPECTS

A. GENERAL REMARKS ON THE DISCRETE POINT SPREAD FUNCTION

In a discrete implementation of the backward-wave reconstruction algorithm, great care has to be taken in order to ensure that the point spread function corresponding to the transfer function used for image reconstruction has a sufficient length.

We assume two apertures, one for the targets D_t and one for the measurement D_m, as depicted in Fig. 4. D_t describes

5. The prefactor j in (18) was omitted because it is irrelevant for image reconstruction.

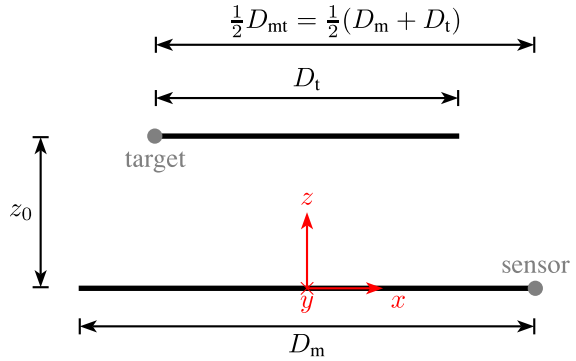

FIGURE 4. Dimensions used for signal processing with the worst case sensor and target positions for the sampling criterion.

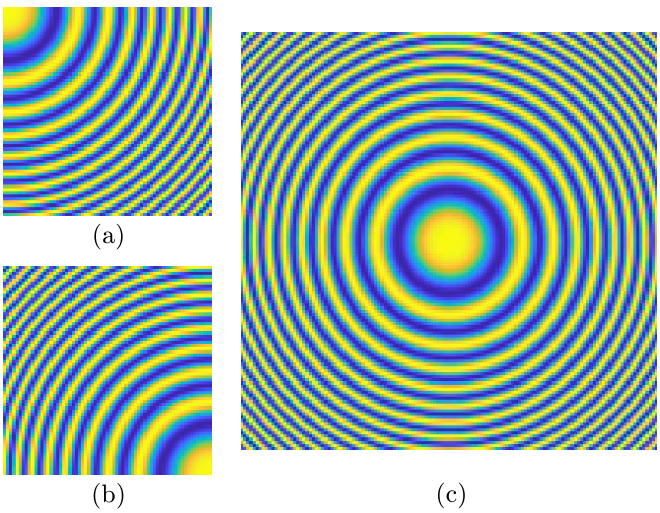

FIGURE 5. Raw aperture data (real part) for two different target positions in (a) and (b), and the required matched filter's impulse response enabling the reconstruction of images from the raw data in (c).

the aperture where reflections are expected, while D_{m} is the width of the scanned aperture. To simplify the following calculations $D_{\mathrm{mt}} = D_{\mathrm{m}} + D_{\mathrm{t}}$ is defined. The two apertures have to be aligned symmetrically along the x and y axes.

Up on closer inspection of Fig. 4 it is obvious that the worst-case distance between a measurement point (sensor location) and a target reflection is $\frac{1}{2}D_{\mathrm{mt}}$. To cover both extreme cases (target left, sensor right and target right, sensor left) the required size of the impulse response has to be at least D_{mt}. The point spread function has to contain "reference information" for every possible position combination within the two aperture limits. Fig. 5 shows simulated measurement data for (a) the target in the top left corner and (b) in the bottom right corner. Measurement and target aperture are assumed to be equal in this example. The impulse response with the minimum size is shown in (c).

B. SPATIAL AND SPATIAL FREQUENCY DOMAIN SAMPLING CRITERIA

For obvious reasons, in discrete implementations of the backward-wave reconstruction algorithm, Nyquist's criterion has to maintained in both the spatial and spatial frequency domain.

In order to develop sampling criteria for both domains, we consider the matched filter (6) used in near-field beamforming and the transfer function of the matched filter (8) used in backward-wave reconstruction again. In the previous section, we found that these two functions represent a Fourier transform pair[6]:

$$e^{+j2k\sqrt{|z_0|^2+x^2+y^2}} \circ\!\!-\!\!\bullet\; e^{+j|z_0|\sqrt{(2k)^2-k_{\mathrm{x}}^2-k_{\mathrm{y}}^2}}. \tag{20}$$

The following analysis will be carried out in terms of the x-axis; however, similar results will apply for the y-axis.

1) SPATIAL DOMAIN SAMPLING CRITERION

In order to determine the spatial sampling requirements imposed by (6), we firstly determine the instantaneous angular spatial frequency in the spacial domain

$$k_{\mathrm{x}}(x) = 2k\frac{d}{dx}\sqrt{x^2+y^2+|z_0|^2} = 2k\frac{x}{\sqrt{x^2+y^2+|z_0|^2}}. \tag{21}$$

By careful inspection of this equation it becomes obvious that the maximum and minimum angular spatial frequencies $k_{\mathrm{x,max}}$ and $k_{\mathrm{x,min}}$ occur if $y = 0$.

Consequently, the maximum instantaneous angular frequency contained within the point spread function is

$$k_{\mathrm{x,max}} = k_{\mathrm{x}}\left(x = \frac{D_{\mathrm{mt}}}{2}\right) = \frac{2k\cdot D_{\mathrm{mt}}}{\sqrt{D_{\mathrm{mt}}^2+4|z_0|^2}}, \tag{22}$$

while the minimum angular frequency calculates

$$k_{\mathrm{x,min}} = k_{\mathrm{x}}\left(x = -\frac{D_{\mathrm{mt}}}{2}\right) = -\frac{2k\cdot D_{\mathrm{mt}}}{\sqrt{D_{\mathrm{mt}}^2+4|z_0|^2}}. \tag{23}$$

Therefore, the point spread function has to cover a minimum angular bandwidth of

$$B_{\mathrm{mt}} = k_{\mathrm{x,max}} - k_{\mathrm{x,min}} = \frac{4k\cdot D_{\mathrm{mt}}}{\sqrt{D_{\mathrm{mt}}^2+4|z_0|^2}}. \tag{24}$$

In order to maintain Nyquist's criterion in the spatial domain

$$\Delta x < \frac{2\pi}{B_{\mathrm{mt}}} = \frac{\lambda}{4}\sqrt{1+4\left(\frac{|z_0|}{D_{\mathrm{mt}}}\right)^2} \tag{25}$$

has to be satisfied,[7] where (24) is used. Δx is the sample interval along the x-axis used during the measurement. In the case of arbitrary large apertures ($D_{\mathrm{mt}} \to \infty$) the right side of (25) converges to $\lambda/4$. To compensate effects caused by the spectral leakage effect the synthesized matched filter's bandwidth is increased by a factor of η_{f}:

$$B_{\mathrm{imp}} = \eta_{\mathrm{f}} B_{\mathrm{mt}}, \tag{26}$$

6. This pair holds for this particular application. The constant scaling factor is ignored.

7. This is the only condition that also applies to the beamforming algorithm.

with $\eta_\mathrm{f} > 1$. This bandwidth corresponds to the synthesized matched filter's bandwidth, although the actual filter's bandwidth might be higher, yet filled with zeros, as will be shown in the following discussion.

One may argue that the sampling criteria for the matched filter's impulse response also needs to be fulfilled:

$$\Delta\tilde{x} < \frac{2\pi}{B_\mathrm{imp}} = \frac{\lambda}{4\eta_\mathrm{f}}\sqrt{1+4\left(\frac{|z_0|}{D_\mathrm{mt}}\right)^2}, \tag{27}$$

where (24) and (26) are used and $\Delta\tilde{x}$ corresponds to the sampling interval of the matched filter's impulse response. The resulting bandwidth of the matched filter's impulse response is then given by[8]

$$B_\mathrm{pad} = \frac{2\pi}{\Delta\tilde{x}}. \tag{28}$$

However, the condition in (27) only applies to the synthesized matched filter's impulse response but not the measurement. Therefore, it is possible to measure with Δx and interpolate the data afterwards to $\Delta\tilde{x}$, such that (27) is satisfied.

2) ANGULAR SPATIAL FREQUENCY DOMAIN SAMPLING CRITERION

In order to establish a similar sampling criterion for the angular spatial frequency domain, we employ an approach which is dual to determining the instantaneous angular spatial frequency as carried out in the previous subsection. This approach seeks to determine the maximum instantaneous distance $x(k_\mathrm{x})$ of the sensor to the target in dependence of the angular frequency. Differentiating the exponent of (8) with respect to k_x similarly to (21) yields

$$x(k_\mathrm{x}) = \frac{d}{dk_\mathrm{x}}|z_0|\sqrt{4k^2-k_\mathrm{x}^2-k_\mathrm{y}^2} = \frac{-|z_0|k_\mathrm{x}}{\sqrt{4k^2-k_\mathrm{x}^2-k_\mathrm{y}^2}}. \tag{29}$$

By careful inspection of this expression it becomes obvious that the maximum and minimum distances between the sensor and the target occur if $k_\mathrm{y} = 0$.

For a given bandwidth B the maximum distance between the sensor and the target in one direction is achieved with the minimum representable angular frequency $-B/2$, and yields

$$x_\mathrm{max} = x\left(k_\mathrm{x} = -\frac{B}{2}\right) = \frac{|z_0|B}{\sqrt{(4k)^2-B^2}}. \tag{30}$$

Following a similar reasoning, the minimum distance is

$$x_\mathrm{min} = x\left(k_\mathrm{x} = \frac{B}{2}\right) = -\frac{|z_0|B}{\sqrt{(4k)^2-B^2}}. \tag{31}$$

Consequently, the minimum required aperture is

$$D_\mathrm{min} = x_\mathrm{max} - x_\mathrm{min} = \frac{2|z_0|B}{\sqrt{(4k)^2-B^2}}. \tag{32}$$

8. This is the complete bandwidth, not the bandwidth actually covered with data. The bandwidth covered with data is B_imp, which is always smaller due to (27).

Inserting the measured signal bandwidth B_min from (24) into (32) yields the minimum required aperture for the impulse response in the spatial domain

$$D_\mathrm{min,sig} = D_\mathrm{mt}. \tag{33}$$

This result is obvious, as D_mt was the initial condition to get the required measurement bandwidth. Although starting from a different perspective, the calculation of the aperture corresponding to this bandwidth, obviously yields the starting point of D_mt.

The result in (33) only includes the properties (bandwidth and aperture) of the measured signal but the synthesized matched filter has a higher bandwidth according to (26), which has to taken into account. Inserting (26) into (32) yields the final requirement for the size of the impulse response:

$$D_\mathrm{imp} = \frac{2|z_0|\eta_\mathrm{f}B_\mathrm{mt}}{\sqrt{(4k)^2-(\eta_\mathrm{f}B_\mathrm{mt})^2}}. \tag{34}$$

By carefully inspection of the denominator of (34) a requirement for the factor η_f follows from

$$(4k)^2 - (\eta_\mathrm{f}B_\mathrm{mt})^2 > 0. \tag{35}$$

With (24) this condition yields

$$\eta_\mathrm{f} < \sqrt{1+4\left(\frac{|z_0|}{D_\mathrm{mt}}\right)^2}. \tag{36}$$

To avoid leakage effects the impulse response's aperture size is increased by a factor η_s:

$$D_\mathrm{pad} = \eta_\mathrm{s}D_\mathrm{imp}, \tag{37}$$

with $\eta_\mathrm{s} > 1$.

3) OVERVIEW

Fig. 6 shows an overview of the implementation aspects which were presented in the previous sections. For a given measurement scenario the target aperture D_t is given. The measurement aperture D_m can theoretically be chosen freely, but larger apertures will result in a higher resolution of final image and are therefore preferred. The sum of both apertures D_mt yields the occupied bandwidth B_mt of the measurement using (24). Equation (25) then provides an upper limit for the measurement interval Δx, which is chosen next. The factor η_f increases the actually synthesized impulse response, according to (26), which will reduce leakage effects in the frequency domain. The value of η_f is limited by (36). Using (27) the bandwidth of the matched filter's impulse response gives a lower limit for the sampling interval $\Delta\tilde{x}$. If $\Delta\tilde{x}$ is chosen different from Δx a resampling of the measured data to $\Delta\tilde{x}$ is required. It is possible to choose $\Delta x = \Delta\tilde{x}$ small enough to satisfy both conditions. This has the benefit that no resampling is required, but the measurement has to be carried out with an unnecessarily high sampling rate, increasing measurement time or system complexity and the amount of data. Once $\Delta\tilde{x}$ is chosen, the complete

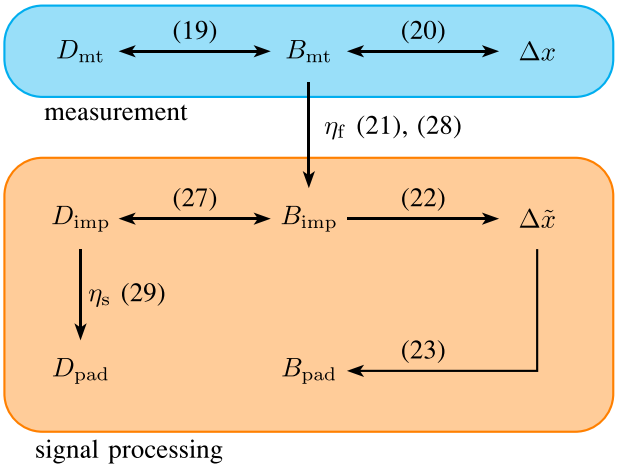

FIGURE 6. Overview of the parameter calculation dependencies for the backward-wave reconstruction algorithm.

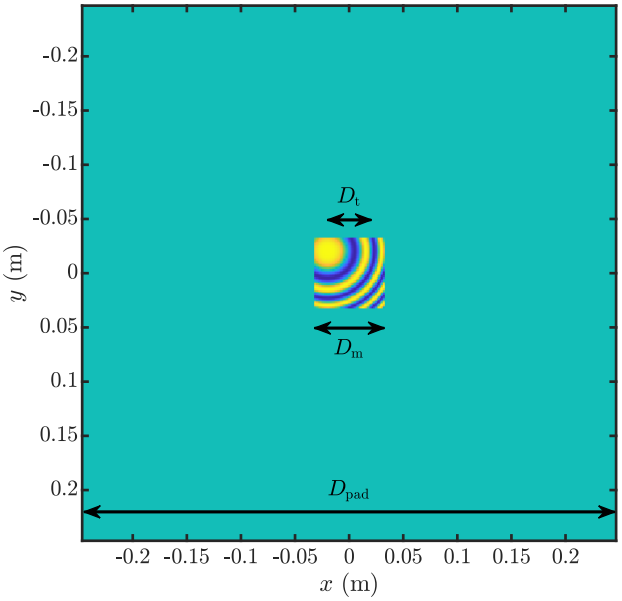

FIGURE 7. Real part of the simulated measurement data in the spatial domain, zero-padded to the final size.

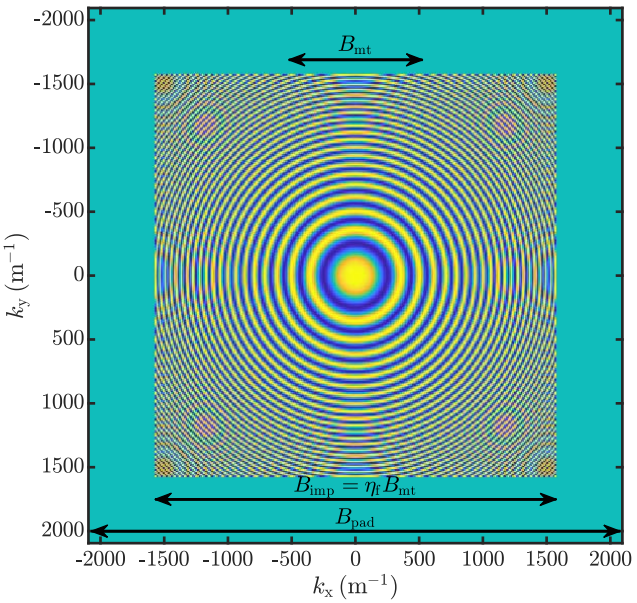

FIGURE 8. Real part of simulated matched filter's impulse response in the spatial frequency domain.

bandwidth B_{pad} of the matched filter's transfer function is given by (28). Equation (34) allows the calculation of the matched filter's impulse response width D_{imp}. This minimum is then again increased by a factor η_{s} to reduce the impact of the leakage effect, resulting in the final padded width D_{pad} with (37). Note that D_{imp} and B_{imp} describe only the used width/bandwidth, while D_{pad} and B_{pad} correspond to the available (i.e., zero-padded) width/bandwidth of the matched filter's impulse response.

V. SIMULATION EXAMPLE

In the following section we will demonstrate the equivalence of near-field beamforming and backward-wave propagation by processing simulated data using implementations of both algorithms. The previously described criteria and boundaries will also be discussed.

The simulation's target aperture D_{t} is 40.5 mm, which is solely defined by the position of the single target at $(-D_{\mathrm{t}}/2,\ -D_{\mathrm{t}}/2,\ z_0)^{\mathrm{T}}$. The measurement aperture D_{m} is chosen to be larger with $D_{\mathrm{m}} = 64.5$ mm, resulting in $D_{\mathrm{mt}} = 105$ mm. Both apertures are multiples of the sampling interval $\Delta\tilde{x}$, which will be introduced later. The measured data and the two apertures are shown in Fig. 7. The distance between these two apertures was set to $z_0 = 0.5$ m. A wavelength of $\lambda = 2.5$ mm (120 GHz) was chosen, as it is the same provided by the measurement system in the following section. The minimum required bandwidth for the measured signal is $B_{\mathrm{mt}} \approx 1050\ \frac{1}{\mathrm{m}}$ from (24), resulting in a maximum value for Δx of 6 mm, according to (25). The upper limit of η_{f} is 9.6 according to (36) and a value of $\eta_{\mathrm{f}} = 3$ is chosen, yielding good results. Therefore, the used bandwidth of the matched filter's impulse response is $B_{\mathrm{imp}} \approx 3149\ \frac{1}{\mathrm{m}}$. As the upper limit for the sampling interval of the impulse response $\Delta\tilde{x}$ in (27) is 2 mm the value for Δx and $\Delta\tilde{x}$ is chosen to be 1.5 mm, providing a slight oversampling in the spacial domain. Choosing both values to be equal removes the interpolation step of the measured data. With $\Delta\tilde{x}$, the padded bandwidth of the impulse response from (28) is $B_{\mathrm{pad}} \approx 4189\ \frac{1}{\mathrm{m}}$. The frequency domain of the matched filter's impulse response is shown in Fig. 8, including the three bandwidths of interest.

The used width of the impulse response is calculated with (34) and yields approximately 33 mm. A value for η_{s} of 1.5 is chosen, yielding good results. η_{s} is used to control the actual width of the impulse response in the spacial domain, ensuring that the correlation of a target at the edge of the target aperture is not carried out right at the edge of the impulse response, which would lead to artifacts due to

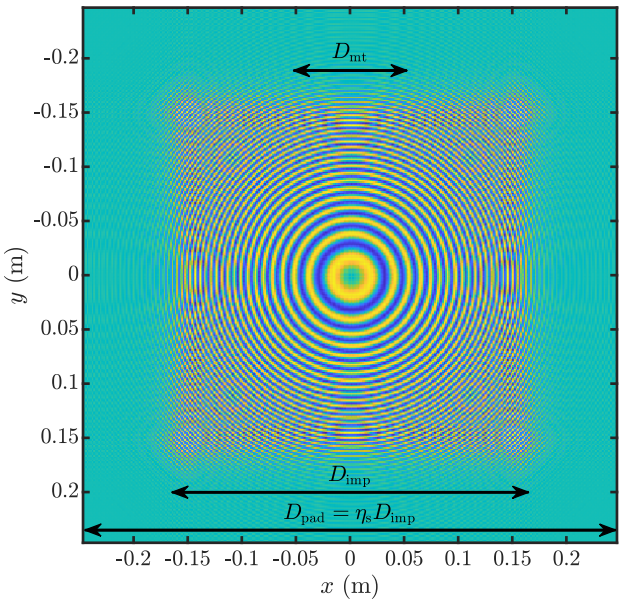

FIGURE 9. Real part of simulated matched filter's impulse response in the spatial domain.

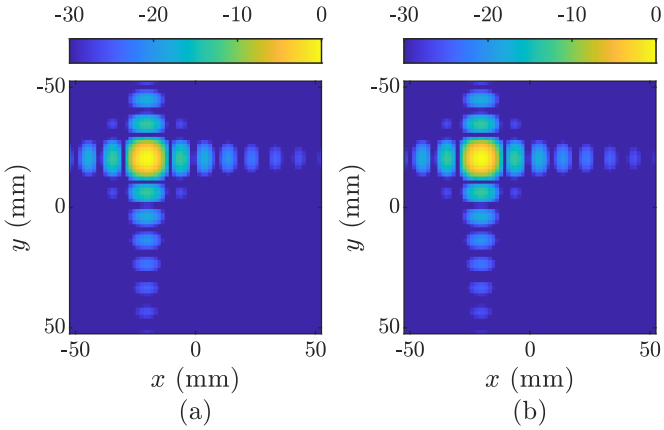

FIGURE 10. 2D comparison between beamforming (a) and backward-wave reconstruction (b) of the simulated data. Both results are normalized to their maximum and given in dB.

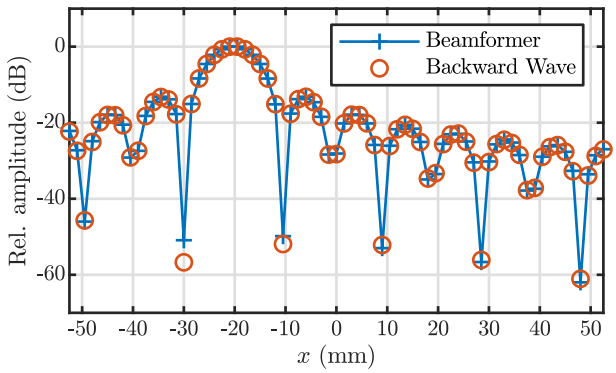

FIGURE 11. Beamforming and backward-wave reconstruction of the simulated data, normalized to their maximum.

TABLE 1. Variable selected for simulation.

Variable	Value	Variable	Value	Variable	Value
D_{m}	64.5 mm	D_{t}	40.5 mm	z_0	0.5 m
$\Delta x = \Delta\tilde{x}$	1.5 mm	η_{s}	1.5	η_{f}	3
D_{mt}	105 mm	D_{imp}	330 mm	D_{pad}	495 mm
B_{mt}	1050 $\frac{1}{\mathrm{m}}$	B_{imp}	3149 $\frac{1}{\mathrm{m}}$	B_{pad}	4189 $\frac{1}{\mathrm{m}}$

the leakage effect. The different apertures and the impulse response in the spatial domain are shown in Fig. 9. The final aperture size of the padded data and the impulse response is $D_{\mathrm{pad}} = 495\,\mathrm{mm}$, as stated by (37). The impulse response and the corresponding aperture values are shown in Fig. 9.

The measured data in Fig. 7 is zero-padded to the final size of the impulse response D_{pad} to allow the multiplication in the frequency domain. The target and measurement apertures are indicated for the x-axis, but also apply to the y-axis as both apertures have the same size. According to (19) the zero-padded data is transformed to the spacial frequency domain with the use of a DFT/FFT, multiplied with the synthesized matched filter in the spatial frequency domain, and the result is transferred back to the spacial domain with the inverse DFT/FFT. The beamforming approach is carried out straight forward according to (3) in the spatial domain.

The results of both approaches are shown in Fig. 10 and Fig. 11 as a one-dimensional cut though the peak reflection. The results match each other almost perfectly, except for very low values. This is expected, as the two factors η_{f} and η_{s} reduce the impact of the leakage effect, but do not eliminate it completely. It is possible to choose higher values for both, yielding better results. The drawback is an increased computational effort required, as more samples need to be processed. The user has to balance between the two goals, depending on the application. All system parameters of the simulation are summarized in Table 1.

VI. MEASUREMENT

To demonstrate both algorithms in a practical application a measurement is carried out using the system previously presented in [13]. It is using a continuous wave radar, operating at 120 GHz or $\lambda \approx 2.5\,\mathrm{mm}$. The radar is mounted on an xy-table, allowing precise positioning of the radar. The positions in the aperture are scanned one after another and combined into a single measurement afterwards. All system parameters are the same as for the simulation in the previous section, given in Table 1. A single corner reflector target with a radar-facing edge length of 29 mm is placed approximately in the center of the aperture in a distance of 0.5 m. Fig. 12 depicts the two results using (a) the beamforming approach and (b) the backward-wave reconstruction algorithm, showing excellent agreement.

VII. CONCLUSION

The equivalence of the two algorithms, near-field beamforming and backward-wave reconstruction, has been shown analytically using two different methods. The proof of equivalence yielded a Fourier pair connecting the spatial and spatial frequency domain for this particular application. From

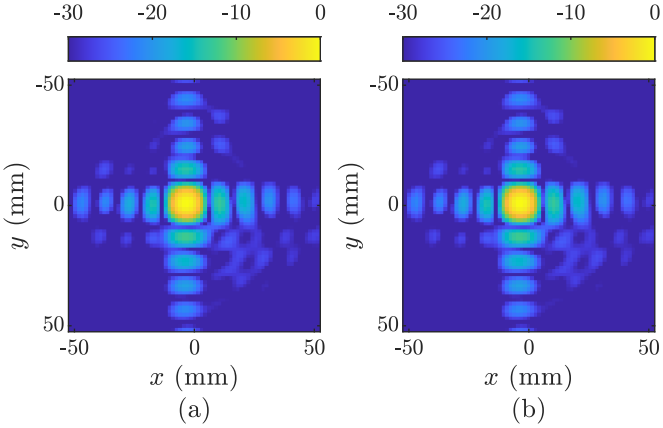

FIGURE 12. Measured scenario with a single target, processed with (a) the beamforming approach and (b) the backward-wave reconstruction. Both results are normalized to their maximum and given in dB.

this Fourier pair we derived several requirements for certain system parameters, like the apertures or the spatial sampling interval, applicable to the backward-wave reconstruction and the beamforming approach. Choosing these parameters wrong will reduce the quality of the resulting image or even break the calculation, as certain parameters will become imaginary. The following discussion lead to two scaling parameters for the matched filter, which are used to reduce the effect of leakage.

A simulation of a scenario was used to exemplarily calculate the required system parameters. Both algorithms were then applied to the generated data and the resulting reconstructed images showed excellent agreement, proving the equivalence of both methods. Lastly, an additional measurement with a 120 GHz non-modulated radar system has been shown, also confirming our findings.

APPENDIX A
PRINCIPLE OF STATIONARY PHASE

The principle of stationary phase [14] is widely used in radar and optics [6] for asymptotic approximation of integrals

$$\int A(x)\, e^{j\phi(x)} \mathrm{d}x = \sqrt{\frac{-\pi}{2\,\phi''(x_0)}} A(x_0) e^{-j\frac{\pi}{4}} e^{j\phi(x_0)} \tag{38}$$

where the stationary point x_0 satisfies $\phi'(x_0) = 0$ [6], [14].

APPENDIX B
ANGULAR SPECTRUM REPRESENTATION OF A SPHERICAL WAVE EMITTED BY A POINT SOURCE

The derivation presented in Section III-B of this paper requires an expansion of a spherical wave emitted by a point source for the free-space' continuous spectrum of plane Eigenmodes.

A. THE WEYL REPRESENTATION

For an inward-traveling (i.e., divergent[9]) spherical wave located at the origin, a well-known possible expansion, which is attributed to Weyl [16], denotes [14], [17]–[19][10]

$$\frac{e^{jkr}}{r} = \frac{j}{2\pi} \iint_{-\infty}^{\infty} \frac{e^{j(k_x x + k_y y + k_z |z|)}}{k_z} \mathrm{d}k_x\, \mathrm{d}k_y \tag{40}$$

where $r = \sqrt{x^2 + y^2 + z^2}$. Note that this expansion is valid for both $z \geq 0$ and $z \leq 0$ [17].

B. MODIFIED ANGULAR SPECTRUM REPRESENTATION

In order to allow for a proper decomposition of (17) into Fourier transforms, an additional substitution $k_x \rightarrow -k_x$ and $k_y \rightarrow -k_y$ is required in (40), which yields

$$\frac{e^{jkr}}{r} = \frac{j}{2\pi} \iint_{-\infty}^{\infty} \frac{e^{j(-k_x x - k_y y + k_z |z|)}}{\sqrt{k^2 - (-k_x)^2 - \left(-k_y\right)^2}} \mathrm{d}k_x\, \mathrm{d}k_y. \tag{41}$$

For a better comparison with the result from Appendix B-C, we expand the right side of equation (41) with 2π and use $k_z = \sqrt{k^2 - k_x^2 - k_y^2}$. Finally we get

$$\frac{e^{jkr}}{r} = \frac{j}{(2\pi)^2} \iint_{-\infty}^{\infty} \frac{2\pi}{k_z}\, e^{-j(k_x x + k_y y - k_z |z|)} \mathrm{d}k_x\, \mathrm{d}k_y \tag{42}$$

provided $k_x, k_y \in \Re$, which is inherently guaranteed.[11]

C. DERIVATION AND ELECTROMAGNETIC INTERPRETATION OF THE MODIFIED ANGULAR SPECTRUM REPRESENTATION

From an electromagnetic point of view, this substitution may be interpreted as using a continuous spectrum of basis functions $e^{-jk_{x_i}x_i}$ rather than $e^{jk_{x_i}x_i}$ for the expansion of the spherical wave into plane waves. Note that both spectra are solutions to the ordinary differential equation

$$0 = \left[\frac{\partial^2}{\partial x_i^2} + k_{x_i}^2\right] \psi_{x_i}, \tag{43}$$

which is obtained by solving the Helmholtz equation for source-free regions $\nabla^2\psi + k^2\psi = 0$ by means of separation of variables if the solution space is assumed to be unbounded in the direction of x_i [15].

The solutions for the ODE's under form of (43) have to maintain the separation condition [15]

$$k^2 = k_x^2 + k_y^2 + k_z^2 \tag{44}$$

and the wavenumber k_z for the direction propagation is calculated as

$$k_z = \begin{cases} \sqrt{k^2 - k_c^2} & 0 < k_c < k \quad \text{Propagating} \\ j\sqrt{k_c^2 - k^2} & k < k_c < \infty \quad \text{Non-propag.} \end{cases} \tag{45}$$

9. In dissipative media where $k = k' - jk''$ applies, the spherical wave diverges for $r \rightarrow \infty$ [15].

10. The cited references denote (40) as

$$\frac{e^{jkr}}{r} = \frac{jk}{2\pi} \iint_{-\infty}^{\infty} \frac{e^{jk(px + qy + m|z|)}}{m} \mathrm{d}p\, \mathrm{d}q. \tag{39}$$

By substituting $k_x = kp$, $k_y = kq$ and $k_z = km$ (40) is obtained if the differential elements are properly substituted ($dp = dk_x/k$ and $dq = dk_y/k$).

11. A comparable substitution is carried out in [17] in order to put the expansion of an outward-traveling (i.e., convergent) spherical wave under a form comparable to (40).

where $k_c^2 = k_x^2 + k_y^2$ shall be referred to as cut-off wavenumber. It is interesting to note that due to the fact that a divergent wave is considered here, we define $k_z = j\sqrt{k_c^2 + k^2}$ for the non-propagating case rather than $k_z = {}^1/_j\sqrt{k_c^2 + k^2}$, which is used for evanescent Eigenmodes in waveguides [15].

In order to further illustrate this electromagnetic interpretation, we will now develop (42) by means of a spherical wave expansion in terms of basis functions $e^{-jk_{x_i}x_i}$. The presented derivation is inspired by the derivations of the Weyl representation (40) given in [17], [18].

The ansatz for the expansion of the spherical wave in terms of the desired basis functions denotes

$$\frac{e^{jkr}}{r} = \iint_{-\infty}^{\infty} a(k_x, k_y) e^{-j(k_x x + k_y y)} e^{+k_z|z|} \, \mathrm{d}k_x \, \mathrm{d}k_y. \quad (46)$$

In the limit $z \to 0$ this becomes

$$\frac{e^{jk\sqrt{x^2+y^2}}}{\sqrt{x^2+y^2}} = \iint_{-\infty}^{\infty} a(k_x, k_y) e^{-j(k_x x + k_y y)} \, \mathrm{d}k_x \, \mathrm{d}k_y. \quad (47)$$

By taking the inverse Fourier transform we obtain

$$a(k_x, k_y) = \frac{1}{(2\pi)^2} \iint_{-\infty}^{\infty} \frac{e^{jk\sqrt{x^2+y^2}}}{\sqrt{x^2+y^2}} e^{j(k_x x + k_y y)} \, \mathrm{d}x \, \mathrm{d}y. \quad (48)$$

for the angular spectrum $a(k_x, k_y)$.

In order to find a closed-form expression for the angular spectrum, we firstly transform this integral to polar coordinates using

$$\rho = \sqrt{x^2 + y^2} \quad k_c = \sqrt{k_x^2 + k_y^2}, \quad (49)$$

where k_c is the cut-off wavenumber. By exploiting the fact that the term $(k_x x + k_y y)$ is a scalar product between the vectors $\langle x, y\rangle$ and $\langle k_x, k_y\rangle$ where ϕ denotes the angle between them, (48) can be rewritten by means of an integral in polar form as

$$a(k_x, k_y) = \frac{1}{(2\pi)^2} \int_0^{2\pi} \int_0^{\infty} \frac{e^{jk\rho}}{\rho} e^{j\rho k_c \cos(\phi)} \rho \, \mathrm{d}\rho \, \mathrm{d}\phi. \quad (50)$$

The integration for ϕ can be performed using the integral representation [20, 9.1.21]

$$J_n(x) = \frac{j^{-n}}{\pi} \int_0^{\pi} e^{jx\cos(\phi)} \cos(n\phi) \, \mathrm{d}\phi \quad (51)$$

for Bessel functions of first kind for $n = 0$, giving[12]

$$a(k_x, k_y) = \frac{1}{(2\pi)^2} \int_0^{\infty} \frac{e^{jk\rho}}{\rho} 2\pi J_0(k_c\rho) \, \rho \, \mathrm{d}\rho. \quad (52)$$

Equation (52) contains a zeroth-order Hankel transform $\mathcal{H}_{n=0}\{\frac{e^{jk\rho}}{\rho}\}$. The corresponding Hankel transform pair (59), which is given in Appendix C, denotes [17], [18]

$$\int_0^{\infty} \frac{e^{ik\rho}}{\rho} J_0(k_c\rho) \, \rho \, \mathrm{d}\rho = \begin{cases} \frac{j}{\sqrt{k^2 - k_c^2}} = \frac{j}{k_z} & 0 < k_c < k \\ \frac{1}{\sqrt{k_c^2 - k^2}} = \frac{j}{k_z} & k < k_c < \infty \end{cases} \quad (53)$$

12. Due to the axial symmetry of the Bessel function $J_0(k_c\rho)$ the remainder of this derivation is equivalent to the derivations of the Weyl representation given in [17], [18].

where the upper case applies for propagating and the lower case for non-propagating parts of the angular wave spectrum.

Inserting (53) in (52) then gives the final expression

$$a(k_x, k_y) = \frac{j}{(2\pi)^2} \frac{2\pi}{k_z} \quad (54)$$

for the angular spectrum. If (54) is inserted into (46), the desired equation (42),

$$\frac{e^{jkr}}{r} = \frac{j}{(2\pi)^2} \iint_{-\infty}^{\infty} \frac{2\pi}{k_z} e^{-j(k_x x + k_y y - k_z|z|)} \, \mathrm{d}k_x \, \mathrm{d}k_y. \quad (55)$$

which is repeated here for clarity, is readily obtained.

D. MODIFIED ANGULAR SPECTRUM REPRESENTATION FOR A POINT SOURCE LOCATED AT AN ARBITRARY POSITION

In order to obtain a similar expansion for a point source located at $\langle x', y', z'\rangle$ rather than at the origin, a substitution $x \to x - x'$, $y \to y - y'$, $z \to z - z'$ is performed in (42). The desired expansion then denotes [19]

$$\frac{e^{jkr}}{r} = \frac{j}{2\pi} \iint_{-\infty}^{\infty} \frac{e^{j(k_x(x'-x) + k_y(y'-y) + k_z|z-z'|)}}{k_z} \mathrm{d}k_x \mathrm{d}k_y \quad (56)$$

where $r = \sqrt{(x-x')^2 + (y-y')^2 + (z-z')^2}$.

APPENDIX C
THE HANKEL TRANSFORM AND RELEVANT HANKEL TRANSFORM PAIRS

The Hankel Transform denotes [21]

$$F_n(s) = \mathcal{H}_n\{f(x)\} = \int_0^{\infty} f(x) J_n(sx) \, x \, \mathrm{d}x \quad (57)$$

where n denotes the transform's order.

By careful analysis of the Hankel transform pair [21, Table 9.1], [22, Tables 1–2]

$$\mathcal{H}_{n=0}\left\{\frac{e^{-\alpha x}}{x}\right\} = \frac{1}{\sqrt{s^2 + \alpha^2}} \quad (58)$$

it can be shown that

$$\int_0^{\infty} \frac{e^{jax}}{x} J_0(sx) \, x \, \mathrm{d}x = \begin{cases} \frac{j}{\sqrt{a^2 - s^2}} & 0 < s < a \\ \frac{1}{\sqrt{s^2 - a^2}} & a < s < \infty \end{cases} \quad (59)$$

follows for $\alpha = -ja$ [17], [18].

REFERENCES

[1] H. Van Trees, *Optimum Array Processing: Part IV* (Detection, Estimation, and Modulation Theory). Hoboken, NJ, USA: Wiley, 2004.

[2] A. L. Boyer, P. M. Hirsch, J. A. Jordan, L. B. Lesem, and D. L. Van Rooy, "Reconstruction of ultrasonic images by backward propagation," in *Acoustical Holography*, A. F. Metherell, Ed. Boston, MA, USA: Springer, 1971, pp. 333–348.

[3] T. Teo and J. Reid, "Some results on wavefield backpropagation," in *Ultrasonics International 87*. London, U.K.: Butterworth-Heinemann, 1987, pp. 72–77.

[4] D. M. Sheen, D. L. McMakin, and T. E. Hall, "Three-dimensional millimeter-wave imaging for concealed weapon detection," *IEEE Trans. Microw. Theory Techn.*, vol. 49, no. 9, pp. 1581–1592, Sep. 2001.
[5] M. E. Yanik and M. Torlak, "Near-field 2-D SAR imaging by millimeter-wave radar for concealed item detection," in *Proc. IEEE Radio Wireless Symp. (RWS)*, Jan. 2019, pp. 1–4.
[6] R. K. Raney, "A new and fundamental fourier transform pair," in *Proc. Int. Geosci. Remote Sens. Symp. (IGARSS)*, vol. 1, May 1992, pp. 106–107.
[7] R. Bamler, "A comparison of range-Doppler and wavenumber domain SAR focusing algorithms," *IEEE Trans. Geosci. Remote Sens.*, vol. 30, no. 4, pp. 706–713, Jul. 1992.
[8] P. Gaydecki, *Foundations of Digital Signal Processing—Theory, Algorithms and Hardware Design*. London, U.K.: IET, 2004.
[9] Y. . Huang and M. Barkat, "Near-field multiple source localization by passive sensor array," *IEEE Trans. Antennas Propag.*, vol. 39, no. 7, pp. 968–975, Jul. 1991.
[10] Y. Shefeng, *Broadband Array Processing*. Berlin, Germany: Springer, 2019.
[11] R. A. Kennedy, T. Abhayapala, D. B. Ward, and R. C. Williamson, "Nearfield broadband frequency invariant beamforming," in *Proc. IEEE Int. Conf. Acoust. Speech Signal Process. Conf.*, vol. 2, 1996, pp. 905–908.
[12] T. H. Cormen, Ed., *Introduction to Algorithms*, 3rd ed. Cambridge, MA, USA: MIT Press, 2009.
[13] F. Schwartau, C. Monka-Ewe, R. Caspary, W. Kowalsky, and J. Schoebel, "A two-dimensional continuous-wave imaging system for scanning of dielectric substrates at millimeter-wave frequencies," in *Proc. Kleinheubach Conf.*, 2019, pp. 1–9.
[14] M. Born and E. Wolf, *Principles of Optics*. Cambridge, U.K.: Pergamon Press, 1959.
[15] R. F. Harrington, *Time-Harmonic Electromagnetic Fields*. New York, NY, USA: IEEE Press, 2001.
[16] H. Weyl, "Ausbreitung elektromagnetischer Wellen über einem ebenen Leiter," *Annalen der Physik*, vol. 365, no. 21, pp. 481–500, 1919.
[17] L. Mandel and E. Wolf, *Optical Coherence and Quantum Optics*. Cambridge, U.K.: Cambridge Univ. Press, 1995.
[18] G. J. Gbur, *Mathematical Methods for Optical Physics and Engineering*. Cambridge, U.K.: Cambridge Univ. Press, 2011.
[19] T. B. Hansen and A. D. Yaghjian, *Plane-Wave Theory of Time-Domain Fields*. New York, NY, USA: IEEE Press, 1999.
[20] M. Abramowitz and I. A. Stegun, *Handbook of Mathematical Functions*. Gaithersburg, MD, USA: Nat. Bureau Stand., 1964.
[21] R. Piessens, "Hankel transform," in *Transforms and Applications Handbook*, A. D. Poularikas, Ed. Hoboken, NJ, USA: CRC Press, 2018, ch. 9, pp. 1–16.
[22] A. Papoulis, *Systems and Transforms With Applications in Optics*. New York, NY, USA: McGraw-Hill, 1968.